

Article

Chitosan/Alginate Nanogels Containing Multicore Magnetic Nanoparticles for Delivery of Doxorubicin

Sérgio R. S. Veloso ^{1,2}, Eva S. Marta ^{1,2}, Pedro V. Rodrigues ³, Cacilda Moura ^{1,2}, Carlos O. Amorim ⁴, Vítor S. Amaral ⁴, Miguel A. Correa-Duarte ⁵ and Elisabete M. S. Castanheira ^{1,2,*}

- ¹ Physics Centre of Minho and Porto Universities (CF-UM-UP), Campus de Gualtar, University of Minho, 4710-057 Braga, Portugal; sergioveloso96@gmail.com (S.R.S.V.)
- ² LaPMET Associate Laboratory, Campus de Gualtar, University of Minho, 4710-057 Braga, Portugal
- ³ Department of Polymer Engineering, Institute for Polymers and Composites (IPC), University of Minho, 4804-533 Guimarães, Portugal
- ⁴ Physics Department and CICECO, Campus de Santiago, University of Aveiro, 3810-193 Aveiro, Portugal; amorim5@ua.pt (C.O.A.); vamaral@ua.pt (V.S.A.)
- ⁵ Centro de Investigación en Nanomateriais e Biomedicina (CINBIO), Universidad de Vigo, 36310 Vigo, Spain
- * Correspondence: ecoutinho@fisica.uminho.pt

Abstract: In this study, multicore-like iron oxide (Fe₃O₄) and manganese ferrite (MnFe₂O₄) nanoparticles were synthesized and combined with nanogels based on chitosan and alginate to obtain a multimodal drug delivery system. The nanoparticles exhibited crystalline structures and displayed sizes of 20 ± 3 nm (Fe₃O₄) and 11 ± 2 nm (MnFe₂O₄). The Fe₃O₄ nanoparticles showed a higher saturation magnetization and heating efficiency compared with the MnFe₂O₄ nanoparticles. Functionalization with citrate and bovine serum albumin was found to improve the stability and modified surface properties. The nanoparticles were encapsulated in nanogels, and provided high drug encapsulation efficiencies (~70%) using doxorubicin as a model drug. The nanogels exhibited sustained drug release, with enhanced release under near-infrared (NIR) laser irradiation and acidic pH. The nanogels containing BSA-functionalized nanoparticles displayed improved sustained drug release at physiological pH, and the release kinetics followed a diffusion-controlled mechanism. These results demonstrate the potential of synthesized nanoparticles and nanogels for controlled drug delivery, offering opportunities for targeted and on-demand release in biomedical applications.

Keywords: nanogels; chitosan; alginate; multicore nanoparticles; magnetic hyperthermia; photothermia; controlled release; doxorubicin; cancer therapy; drug delivery



Citation: Veloso, S.R.S.; Marta, E.S.; Rodrigues, P.V.; Moura, C.; Amorim, C.O.; Amaral, V.S.; Correa-Duarte, M.A.; Castanheira, E.M.S. Chitosan/Alginate Nanogels Containing Multicore Magnetic Nanoparticles for Delivery of Doxorubicin. *Pharmaceutics* **2023**, *15*, 2194. <https://doi.org/10.3390/pharmaceutics15092194>

Academic Editors: Rita Muzzalupo and Xiaowei Zeng

Received: 17 July 2023

Revised: 13 August 2023

Accepted: 22 August 2023

Published: 24 August 2023



Copyright: © 2023 by the authors. Licensee MDPI, Basel, Switzerland. This article is an open access article distributed under the terms and conditions of the Creative Commons Attribution (CC BY) license (<https://creativecommons.org/licenses/by/4.0/>).

1. Introduction

Nanogels are nanoscale three-dimensional networks with the ability to adsorb a large amount of water [1]. Typically, these structures range in size from 10 to 200 nm and exhibit a high degree of hydrophilicity, as well as a tuneable size and composition. The small size enables the nanogels to preferentially accumulate in tumors by leveraging the enhanced permeabilization and retention (EPR) effect. Moreover, the nanogels' biocompatibility, biodegradability, and ability to encapsulate a broad variety of bioactive molecules make them attractive for drug delivery applications [2–5].

Polysaccharides and proteins are among the most commonly utilized natural polymers for the development of nanogels [1,2,6,7]. For instance, Wang et al. [2] created bovine serum albumin (BSA)@chitosan nanogels capable of encapsulating doxorubicin (DOX) with an entrapment ratio of 46.3%. The system provided sustained drug release and lower cytotoxicity than using DOX alone. In particular, chitosan, a cationic, naturally derived polysaccharide from chitin, has been an attractive choice in the development of nanogels for the delivery of numerous drugs, such as DOX [8–12], curcumin (CUR) [13,14], 5-fluorouracil [15], and paclitaxel [16].

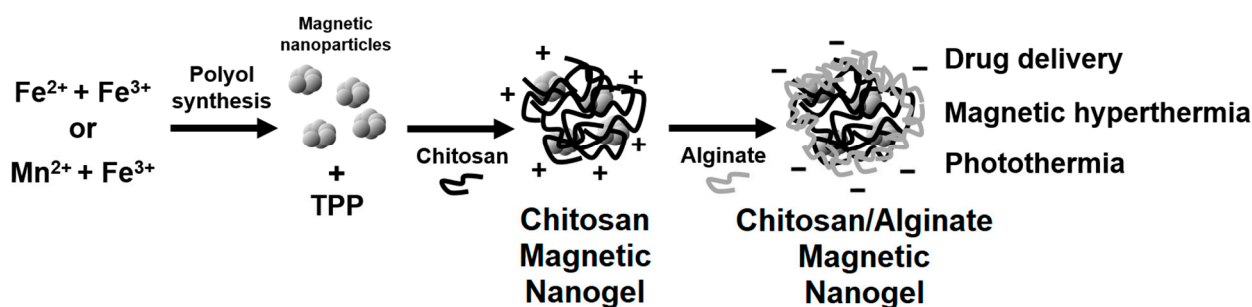
Chitosan particles possess a positively charged surface that can be coated with polyanions, such as alginate, via electrostatic interactions. This has been shown to improve the stability in physiological conditions and reduce the cytotoxicity, which are both required for further progressing to in vitro and/or in vivo studies [6,7,17–19].

The addition of magnetic nanoparticles provides the system with theranostic properties, such as magnetic targeting, magnetic hyperthermia, and the ability to serve as contrast agents or magnetic particle imaging tracers for imaging techniques [20–25]. Furthermore, the presence of magnetic nanoparticles can synergistically enhance the efficacy of cancer therapy through magnetic hyperthermia and photothermia using near-infrared (NIR) laser light irradiation [26–30]. The photothermia effect of iron oxide nanoparticles through NIR laser irradiation has been successful against different cancer cell types [30], and the particles are reported to attain a high energy conversion efficiency [31].

The majority of the reported works on magnetic nanogels focus on synthetic polymers [23], since tailoring polymer structure provides more flexibility in achieving the desired properties for biomedical applications. However, the synthetic polymers have limitations regarding the biodegradability, biocompatibility, and toxicity, and some preparation methods lack scalability [32–34]. On the other hand, the natural polymers can offer advantages over the synthetic polymers by overcoming the mentioned limitations, besides being obtained from abundant renewable sources and displaying a high binding capacity for various drugs [35,36].

Doxorubicin (DOX) is an anthracycline known to function as a DNA intercalating agent and to inhibit topoisomerase II [37]. This powerful chemotherapy drug is widely used to treat several cancers, including breast, ovary, lung, bladder, and multiple myeloma [38]. However, a significant challenge lies in its lack of specificity, which restricts the administration of higher therapeutic dosages, as it may lead to dose-dependent side effects, such as myelosuppression and cardiotoxicity [38]. To address these limitations, doxorubicin can be encapsulated in nanoformulations, enabling the controlled and targeted delivery to the desired site, resulting in improved therapeutic efficacy and reduced off-target toxicity. In particular, magnetic nanogels have emerged as a promising drug delivery system due to their ability to minimize premature drug release, besides enabling the magnetic targeting and synergistic effect of thermo-chemotherapy [38,39].

This work aimed to develop self-assembled magnetic nanogels based on alginate and chitosan for the delivery and controlled release of doxorubicin. Firstly, the multi-core magnetic nanoparticles of manganese ferrite and magnetite were synthesized and compared, considering the high heating efficiency that can be achieved through photothermia [27,40,41]. The system was prepared through self-assembly using an entirely water-based procedure (Scheme 1). The method consisted in initially dispersing magnetic nanoparticles in a triphosphosphate (TPP) solution, which is then added to a chitosan solution. Finally, the surface charge of the nanogels is made negative through the addition of an alginate solution. The influence of coating the nanoparticles with citrate was assessed to evaluate the tuneability of the gels' size and encapsulation efficiency, as a negatively charged surface might favor the adsorption of the positively charged doxorubicin. Additionally, the functionalization with BSA, as a means for assessing the tuneability of the nanoparticles' size and inclusion of hydrophobic cavities, was also explored. The developed nanogels were tested for the release of doxorubicin in different conditions, and the possibility of using photothermia to enhance its release was also studied.



Scheme 1. Schematic representation of the developed self-assembled chitosan/alginate magnetic nanogels.

2. Materials and Methods

2.1. Synthesis of Nanoparticles and Development of Magnetic Nanogels

2.1.1. Synthesis of Magnetic Nanoparticles (NPs)

Magnetic nanoparticles of magnetite and manganese ferrite were synthesised by a method adapted from Bertuit et al. [40] and Hugouenq et al. [42]. Briefly, FeCl₃·6H₂O (2 mmol, 2 equiv) and FeSO₄·7H₂O or MnSO₄·H₂O (1 mmol, 1 equiv) were dissolved overnight in a mixture of DEG (20 mL) and NMDEA (20 mL) under a N₂ inert atmosphere. Simultaneously, NaOH pellets (8 mmol, 8 equiv) were ground and dissolved overnight in a mixture of DEG (10 mL) and NMDEA (10 mL). After 30 min under a N₂ inert atmosphere, the two solutions were mixed via magnetic stirring for 1 h, still under a N₂ inert atmosphere. A total of 250 µL of ultrapure water was added, and the solution was then heated to 220 °C (reflux), in which the rate between 60 °C and 220 °C was 10 °C/5 min. After a holding temperature of 1 h, the solution was allowed to cool down to room temperature. The suspension was diluted in ethanol and washed two times through centrifugation with ethanol (20 min, 9000 g). The black solid was dried at 100 °C and later redispersed in water.

2.1.2. Citrate Functionalized Magnetic Nanoparticles (NPs@BSA)

Magnetic nanoparticles were functionalized with citrate as described elsewhere [43]. In summary, 50 mg of NPs were dispersed in 10 mL of trisodium citrate 0.3 M at pH = 7, and sonicated for 30 min. Then, the solution was stirred at 80 °C for 2 h, washed with water:acetone 1:1, and stored in water for further use. The synthesized particles' size was measured through Transmission Electron Microscopy (TEM), and the functionalization was evaluated through Dynamic Light Scattering (DLS) measurements of the hydrodynamic diameter and zeta potential.

2.1.3. Synthesis of Bovine Serum Albumin Functionalized Magnetic Nanoparticles (NPs@BSA)

For the functionalization with BSA, EDC (0.1 mg EDC/mg NP) was initially dissolved in a dispersion of citrate-functionalized magnetic NPs (2 mg/mL) under stirring at room temperature. Then, some amount of BSA was added for the appropriate final concentration (0.8, 2.4, or 4 mg/mL), and the reaction was left stirring for 24 h. The NPs@BSA were separated by centrifugation at 9000 g for 30 min and washed with deionized water. Finally, the nanoparticles were redispersed and stored in water at 4 °C.

2.1.4. Development of Magnetic Nanogels

Magnetic nanogels were developed through a method adapted from Schütz et al. [6]. Briefly, a 0.1 w/v% chitosan (448869, Sigma-Aldrich, Reykjavik, Iceland, low molecular weight, 75–85% deacetylation) solution was prepared by dissolving chitosan in ultrapure water and gradually adding 1 M HCl until the pH stabilized between 3.5 and 4.0. Subsequently, 0.1 w/v% tripolyphosphate (TPP) solution was added dropwise to a 9-fold volume of chitosan solution with vigorous stirring. To obtain magnetic nanogels, the nanoparticles were dispersed in the TPP solution for a concentration of 2 mg/mL. The mixture was stirred for at least 1 h. For addition of doxorubicin, a 0.1 w/v% TPP solution with 200 µM of doxorubicin was employed.

For the surface decoration with alginate (180947, Sigma-Aldrich), the above formulation was diluted 1:1 with ultrapure water. The resulting nanogel dispersion was then added dropwise to a 0.1 *w/v*% sodium alginate solution in a ratio 1:1 under strong agitation. The pH was maintained between 7.1 and 7.5 by adding 0.025 M NaOH. Afterward, the dispersion was washed at 3500 g for 10 min with deionized water and finally stored in 500 μ L of water at 4 °C.

2.2. Characterization Techniques

2.2.1. General Spectroscopic Methods

Absorption spectra were recorded using a Shimadzu UV-3600 Plus UV-Vis-NIR spectrophotometer (Shimadzu Corporation, Kyoto, Japan). X-ray diffraction (XRD) analyses were conducted with a conventional PANalytical X'Pert PRO diffractometer (Malvern Panalytical Ltd., Malvern, UK), utilizing Cu K α radiation, in a Bragg–Brentano configuration at the Electron Microscopy Unit, University of Trás-os-Montes and Alto Douro (UTAD), Vila Real, Portugal. Raman spectroscopy measurements were performed at room temperature using a LabRAM HR Evolution confocal microscope system (HORIBA France SAS, Palaiseau, France), equipped with a high-resolution grating of 1800 grooves mm⁻¹. The excitation line, 532 nm, of an NIR diode laser was focused onto the sample by a $\times 50$ objective with a numerical aperture (NA) value of 0.80 in a backscattering geometry. The spectra were acquired with a measured power of about 1.43 mW on the sample, with a spectral acquisition time of 5 s averaged over 10 accumulations and the range 100–1000 cm⁻¹. The average hydrodynamic diameter and zeta potential of the nanoparticles (*n* = 3 independent runs) were measured in phosphate buffer pH 7.4 at 0.01 mg/mL in a Dynamic Light Scattering (DLS) equipment Litesizer™ 500 from Anton Paar (Anton Paar GmbH, Graz, Austria), using a semiconductor laser diode of 40 mW and λ = 658 nm, a backscatter angle (175°), and a controlled temperature of 25 °C.

2.2.2. Transmission Electron Microscopy (TEM)

Nanoparticles' TEM images were captured using a high contrast JEOL JEM-1010, operating at 100 kV (CACTI, Vigo, Spain). For the STEM images, a NanoSEM—FEI Nova 200 was used, operating at 15 kV, coupled to an Electron Dispersive Spectroscopic analyzer (EDS) and Electron Backscatter Diffraction EDAX—Pegasus X4M analyser and detection system (EBSD) at SEMAT/UM (Serviços de Caracterização de Materiais, Guimarães, Portugal). A small portion of the sample was placed onto a TEM 400 mesh copper grid with Formvar/Carbon (ref. S162-4 from Agar Scientific, London, UK), held by tweezers, and the excess solution was cleaned. The processing of STEM images was performed using ImageJ software (National Institutes of Health, NIH, Bethesda, MD, USA, version 1.53t), which consisted of enhancing local contrast and adjusting brightness followed by manual selection of nanoparticles/nanogels.

2.2.3. Magnetic Properties

Magnetic measurements were performed in an MPMS3 SQUID magnetometer (Quantum Design Inc., San Diego, CA, USA). The field-dependent magnetization (hysteresis cycles) of the samples were measured in the large field range (up to *H* = 5570.42 kA/m or *B* = 7 T) for each sample. In all the cases at 300 K, given the room temperature applications they are designed for, a specific magnetic field correction for the trapped flux in the superconducting coil was conducted, achieving an accuracy of residual less than 0.16 kA/m [44].

2.2.4. Magnetic Hyperthermia Measurements

With the aim of evaluating the heating performance, magneto-caloric measurements were carried out using a hyperthermia system magneTherm (nanoTherics, Warrington, UK), working at *f* \approx (162, 271, 383, 617) kHz and at the magnetic field *H* = (13.56, 12.76, 9.57) kA/m. For all experiments, the initial temperature was stabilized before starting the

measurement. Next, the AC magnetic field was applied for 10 min, and the temperature variation was recorded using a thermocouple.

A phenomenological Box–Lucas equation was fitted to the temperature variation over time ($\Delta T(t)$) profiles during exposure to the alternating magnetic field. The equation is described by the parameter A (saturation temperature) and B (related with the curvature of the profile) as follows:

$$\Delta T(t) = A(1 - e^{-Bt}) \quad (1)$$

The product $A \times B$ at $t = 0$ is equivalent to the ratio of the initial slope of the temperature curves, dT/dt , required to calculate SLP , which is defined as follows:

$$SLP = \frac{m_{sample}c}{m_{NP}} \frac{dT}{dt} \quad (2)$$

where m_{sample} is the total mass of the sample (g), c is the specific heat capacity of the sample (approximated to $c_{water} = 4.185$ J/g/K), and m_{NP} is the total mass of nanoparticles in the sample (g).

2.2.5. Photothermia Measurements

To obtain the photothermia profiles upon irradiation of the nanoparticles, the sample (2 mL) was prepared in a 1 cm polystyrene cuvette, placed in a sample cuvette holder with the temperature stabilized at 37 °C, and irradiated with an 808 nm laser (1 W/cm²). The temperature was measured by placing a K-type thermocouple 1 cm inside the sample.

The light-to-heat conversion efficiency was calculated from the equation [45]:

$$\eta = B \cdot \Delta T \cdot \frac{m_{sample}c}{P_0(1 - 10^{-A})} \quad (3)$$

where ΔT is the temperature variation, m_{sample} is the total mass of the sample, c is the specific heat capacity of the sample (approximated to $c_{water} = 4.185$ J/g/K), P_0 is the incident laser power, A is the sample absorbance, and B is the constant rate of heat dissipation from the solution to the external environment, which is measured during heat relaxation as $e^{-Bt} = \frac{T(t) - T_0}{T_m - T_0}$, in which $T(t)$ is the temperature measured at time t , T_0 is the starting temperature, and T_m is the maximum temperature. The value of B was determined to be 0.0035 ± 0.0002 s⁻¹.

2.3. Swelling Assays

The nanogels were subjected to swelling experiments by immersing them in phosphate buffer 0.1 M pH = 7.4 for 72 h. At specific time intervals, the nanogels were centrifuged and weighed (W_s). Afterward, the nanogels were dried and weighed again (W_0). To determine the swelling ratio, the following equation was used:

$$SR = \frac{(W_s - W_0)}{W_0} \quad (4)$$

2.4. Doxorubicin Loading and Release Assays

Nanogels loaded with doxorubicin were prepared by initially employing a 0.1 w/v% TPP solution containing 200 μM of doxorubicin. The supernatant obtained from the centrifugation of the nanogels was stored and its fluorescence measured to determine the non-encapsulated doxorubicin. The encapsulation efficiency was determined as follows:

$$EE(\%) = \frac{(amount_{total} - amount_{non-encapsulated})}{amount_{total}} \times 100 \quad (5)$$

For the release assays, 100 μL of the nanogels dispersion (500 μL at a nanogel concentration of ~ 6 mg/mL) were added to microcentrifugal tubes. Then, phosphate buffer 0.1 M pH = 7.4 or 6 (700 μL) was added to keep pH constant; an Amicon[®] Ultra-0.5 mL centrifugal filter with 0.1 μm pore size was immersed and was filled with 200 μL of buffer (top reservoir). Aliquots were taken and replaced with fresh buffer, and fluorescence ($\lambda_{exc} = 480$ nm) was measured to determine the concentration at each time point. For the assays with laser irradiation at 808 nm (1 W/cm²), the samples were irradiation for 10 min after each aliquot. Release profile assays were performed in triplicate.

3. Results and Discussion

3.1. Characterization of the Magnetic Nanoparticles

The synthesized nanoparticles displayed a flower-like morphology, which is in line with the morphologies obtained for iron oxide particles through the employed polyol synthesis [40,46,47]. The iron oxide and manganese ferrite nanoparticles were obtained with an average physical diameter of 20 ± 3 nm and 11 ± 2 nm (Figure 1A,B and Figure S1), respectively, and with low size polydispersity, as determined from the analysis of TEM images (N = 300). The size of the magnetite nanoparticles was in line with other reported sizes of multicore particles obtained through the same method [40,42,47], while the use of Mn(II) resulted in smaller particle sizes.

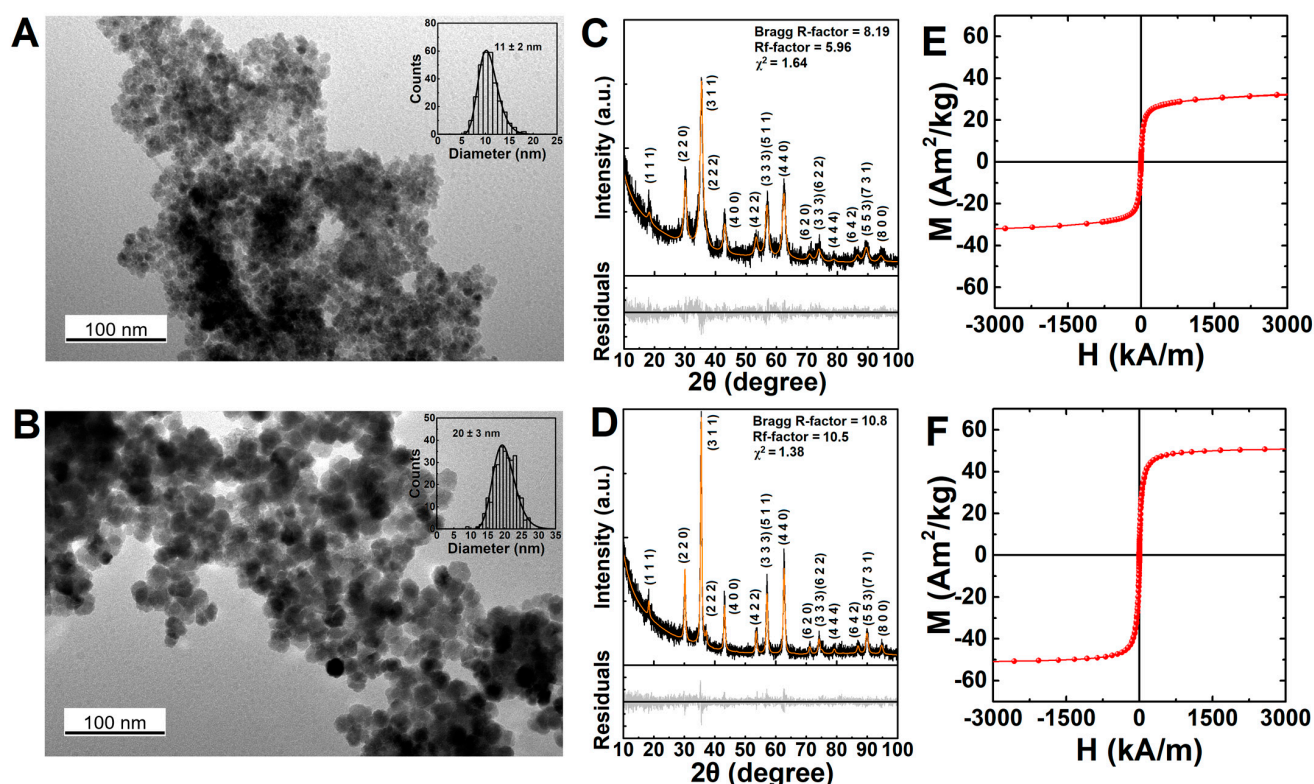


Figure 1. TEM images of the (A) MnFe_2O_4 nanoparticles and (B) Fe_3O_4 nanoparticles. Inset: Histograms of the particle sizes measured in the respective samples. XRD diffraction pattern and fitted Rietveld refinement pattern of the (C) MnFe_2O_4 and (D) Fe_3O_4 nanoparticles. Magnetization dependence on the applied magnetic field measured at 300 K for (E) MnFe_2O_4 nanoparticles and (F) Fe_3O_4 nanoparticles.

The X-ray diffraction (XRD) patterns in Figure 1C,D suggested the crystalline nature of the synthesized nanoparticles and displayed the Bragg's reflections characteristic of the Fd-3m space group, as highlighted in the diffractogram [48,49]. Rietveld analysis was performed using a phase adapted from a CIF file of iron oxide (CIF file 2300618, space group

Fd-3m). The refinement resulted in a good quality fitting, as indicated from the parameters R_f and χ^2 included in Figure 1C,D. An average crystallite size of 6 nm and 14 nm was obtained for manganese ferrite and magnetite nanoparticles, respectively. The smaller crystalline size obtained from XRD can be associated with the misalignment between the grains that arise from crystalline defaults at the grain interfaces [42]. Additionally, the lattice parameter of 8.413 Å was calculated for the manganese ferrites, and 8.381 Å for the magnetite nanoparticles, which are in agreement with the commonly reported values [40,48,50–52]. The magnetite nanoparticles were also confirmed to not be oxidized, as suggested by the presence of a band above 1000 nm, associated with the intervalence charge transfer between Fe^{2+} and Fe^{3+} in magnetite (Figure S2) [53].

Regarding the magnetic properties, the magnetite nanoparticles ($51.1 \text{ Am}^2/\text{kg}$) displayed larger saturation magnetization than the manganese ferrite ($33.8 \text{ Am}^2/\text{kg}$), thus indicating the detrimental effect of replacing Fe(II) with Mn(II) in the employed synthesis method. Nonetheless, both displayed an $M_r/M_s < 0.1$ (Table S1), which suggests that both nanoparticles are superparamagnetic [54].

In solution, the manganese ferrite nanoparticles' larger hydrodynamic diameter ($247 \pm 15 \text{ nm}$) compared with the magnetite nanoparticles' ($148 \pm 1 \text{ nm}$) may be associated with the smaller zeta potential ($<30 \text{ mV}$) leading to aggregation, which is also suggested by a larger polydispersity index (Figure S3 and Table S2).

3.2. Assessment of the Magnetic Nanoparticles for Photothermia

Both MnFe_2O_4 and Fe_3O_4 nanoparticles displayed high heating generation upon laser irradiation at 808 nm ($1 \text{ W}/\text{cm}^2$), as displayed in Figure 2. Notably, the Fe_3O_4 nanoparticles could induce a temperature change of $\sim 12^\circ\text{C}$ in 6 min at a concentration of 1 mg/mL. This strong enhancement in temperature variation can be associated with the clustering of the nanoparticles at high concentrations [31,55].

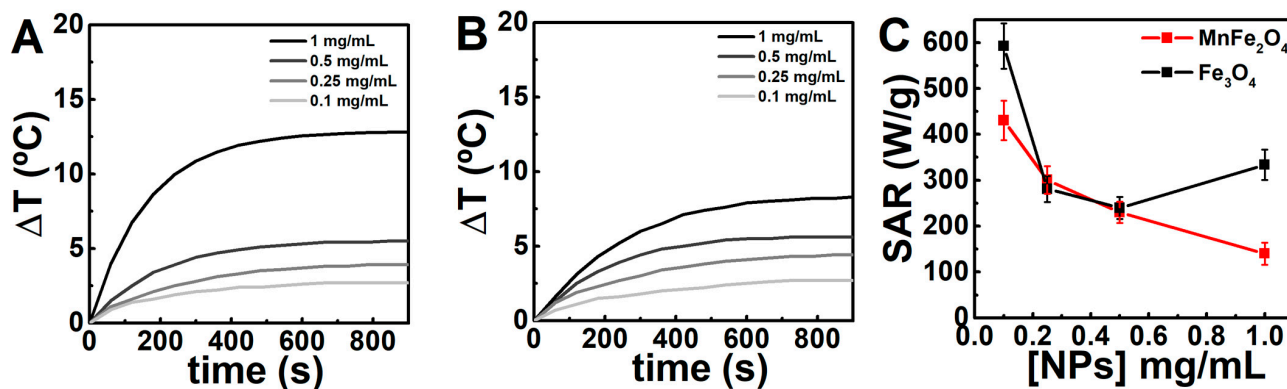


Figure 2. Temperature variation profiles of different concentrations of the (A) Fe_3O_4 and (B) MnFe_2O_4 nanoparticles upon laser irradiation at 808 nm with power density of $1 \text{ W}/\text{cm}^2$. (C) Dependence of the specific absorption rate (SAR) on the nanoparticle concentration.

The stronger heating efficiency of the Fe_3O_4 nanoparticles is also indicated by the calculated specific absorption rate (SAR), which displayed a value of $\sim 600 \text{ W}/\text{g}$ at $0.1 \text{ mg}/\text{mL}$. The high heating efficiency might result from the larger mean volume of the Fe_3O_4 nanoparticles and the lower concentration of defects [40]. Regarding the latter, an Urbach energy (E_U) of 1.3 eV and 1.1 eV was obtained for the Fe_3O_4 and MnFe_2O_4 nanoparticles, respectively (Figure S4). Smaller E_U values correspond to high-defect systems, and consequently, are associated with a decrease in heating efficiency [40]. However, the SAR values can also be linked to the mean hydrodynamic size [56], as the concentration affects the laser beam diffusion. In this sense, the lower mean hydrodynamic size of the Fe_3O_4 nanoparticles might contribute to its higher SAR value, compared with the MnFe_2O_4 nanoparticles. In addition, as reported in other studies [41,45,55], the SAR value decreases

with the nanoparticle content as a result of the light absorption of the colloidal suspension. This can be understood in terms of the Lambert–Beer’s law, i.e., the unequal distribution of the incident light, which is mainly absorbed and scattered in the front of the cuvette, leads to a gradient in the incident power [31]. Hence, as the light absorption is not homogenous along the nanoparticle’s suspension, the heat release will also be inhomogeneous. Additionally, a photothermal conversion efficiency (η) of $33 \pm 4\%$ and $20 \pm 3\%$ was obtained for the Fe_3O_4 and MnFe_2O_4 nanoparticles, respectively, which are comparable to or overcome other reported nanoparticles [31,41,45,55]. In particular, the obtained value for the Fe_3O_4 nanoparticles is in line with the commonly reported heating efficiencies for iron-based nanomaterials [40,55,57]. The magnetic hyperthermia was also assessed (Figure S5), but the heating efficiency was lower than photothermia, as described in other works [31,45].

3.3. Functionalization of the Nanoparticles

In this work, the functionalization with citrate and BSA was studied to understand if a small negatively charged molecule or additional hydrophobic cavities [58–60], respectively, could improve the drug encapsulation. Additionally, the encapsulation of proteins, namely with biological activity, can be of potential interest for biomedical applications. The coating with citrate resulted in a decrease in the hydrodynamic diameter, a negative zeta potential (around -20 mV) at $\text{pH} = 7.4$, and a polydispersity index (PDI) within the 0.1–0.2 range, which is indicative of good stability and less aggregation compared with the uncoated nanoparticles. For simplicity, the remaining studies with BSA were carried out with one of the magnetic nanoparticles (Fe_3O_4). The functionalization with BSA led to an incremental increase in the hydrodynamic size, a low PDI, and a largely unchanged zeta potential across the different preparations but was less negative than the citrate-stabilized nanoparticles. The correlograms and UV-vis absorption spectra are included in the Supplementary Information (Figures S6 and S7).

The absorption spectra profiles of the nanoparticles were similar, in which the different intensities could be related with the particle size (Figure S7). In Figure 3C, commonly reported Raman shifts for citrate [61–65] and BSA [66,67] are highlighted, which further confirms the coupling of citrate and BSA to the particles. The spectrum of citrate-functionalized nanoparticles showed modes near 1080 cm^{-1} (ν_{CC} symmetric), 1190 cm^{-1} (ν_{CCO}), and 1610 cm^{-1} ($\nu_{\text{CO}_2^-}$ asymmetric), as well as a peak near 1500 cm^{-1} that could be associated with the stretching vibration mode of the carboxylate groups. The presence of BSA resulted in additional peaks, mainly a mode of about 1450 cm^{-1} that can be assigned to the δCH_2 .

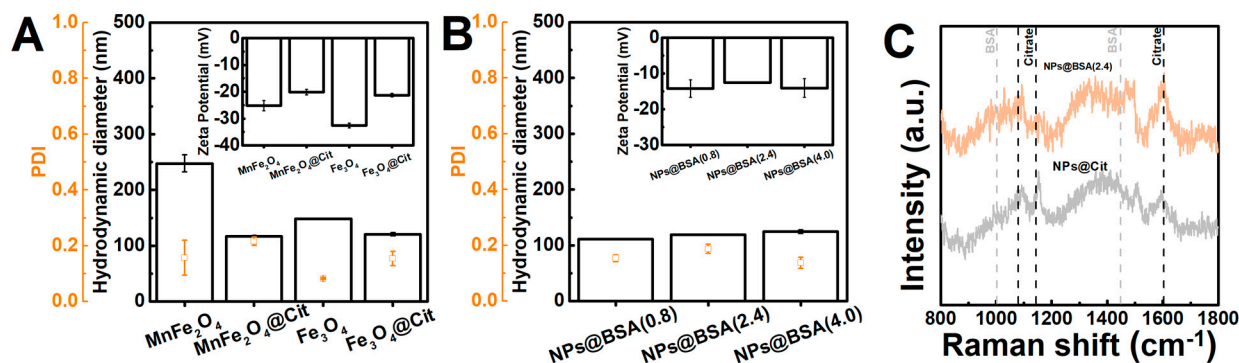


Figure 3. Hydrodynamic diameter (bars) and polydispersity index (PDI, squares) of the (A) bare and the citrate-stabilized nanoparticles, and (B) of the BSA-functionalized Fe_3O_4 nanoparticles. Insets: zeta potential of the respective nanoparticles. The particles functionalized with BSA were labelled $\text{NPs}@BSA(x)$ (where $x = 0.8, 2.4$, and 4.0), corresponding to reaction with 0.8, 2.4, and 4 mg/mL of BSA. (C) Raman spectra of Fe_3O_4 nanoparticles functionalized with citrate and BSA.

3.4. Characterization of the Nanogels

Nanogels were prepared for all particle formulations, including neat nanogels (i.e., nano-hydrogels, NHG). Overall, the resulting nanogels displayed a good polydispersity, a strongly negative zeta potential in pH = 7.4 0.1 M phosphate buffer (around -25 mV), and a size larger than 200 nm, which is consistent with the results reported in [6]. In particular, the polydispersity index (PDI) remained within the range of 0.1–0.2, which is considered an acceptable value for drug delivery applications [68]. As alginate consists of alternating blocks of β -(1 \rightarrow 4)-linked-D-mannuronic acid and α -(1 \rightarrow 4)-linked-L-glucuronic acid [35], the nanogels are endowed with a negative surface charge.

Noticeably, the BSA-functionalized nanoparticles led to nanogels with a slightly larger hydrodynamic diameter, which can result from the aggregation of these nanoparticles during the preparation, as the zeta potential was lower than the other particles. Additionally, the functionalization with citrate resulted in nanogels with a hydrodynamic diameter similar to the nanogels and smaller than when bare nanoparticles are employed, which might result from the favourable electrostatic interactions between the surface citrate carboxyl moieties and the chitosan positively charged amine groups. A smaller size was also obtained for nanogels with citrate-stabilized MnFe_2O_4 nanoparticles (Figure S8).

The encapsulation of nanoparticles into nanogels was also evaluated through Raman spectroscopy. In Figure 4C, commonly reported Raman shifts for chitosan [69] and alginate [70,71] are highlighted, as well as the mentioned BSA and citrate Raman shifts. The nanogels displayed some peaks indicative of the nanoparticles being covered with the polysaccharides, such as a strong broad peak around 1600 cm^{-1} that includes contributions from δNH_2 and νCO_2^- modes, as well as the vibrational modes of the remaining components (BSA and/or citrate).

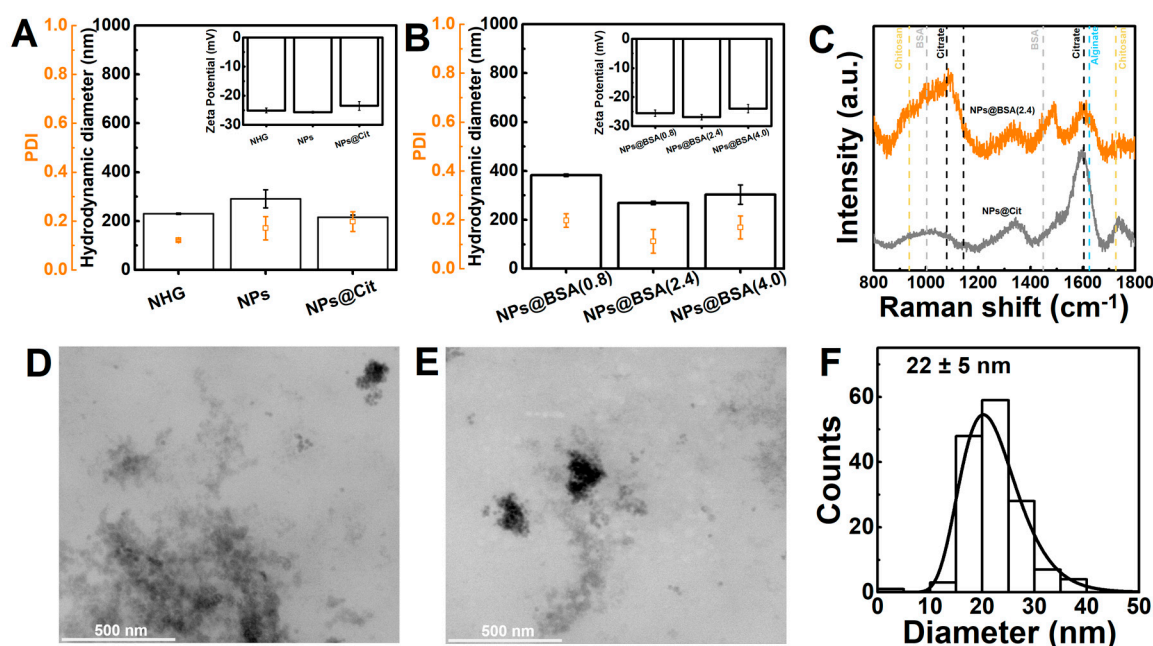


Figure 4. Hydrodynamic diameter (bars) and polydispersity index (PDI, squares) of the (A) nanogels prepared with bare and the citrate-stabilized Fe_3O_4 nanoparticles, and (B) of the BSA-functionalized nanoparticles. Insets: zeta potential of the respective nanogels. (C) Raman spectra of nanogels containing Fe_3O_4 nanoparticles functionalized with citrate and BSA. (D,E) TEM images of the nanogels containing citrate-stabilized Fe_3O_4 nanoparticles, and (F) the respective histogram of the measured particle size.

Regarding the swelling capability, all the nanogel formulations exhibited fast swelling within the first 3 h, reaching equilibrium after 4 h (Figure S9). The swelling curves could

be described by a second-order kinetic model [72], and the fitting of Korsmeyer–Peppas power law suggested that the water transport is driven by a diffusion-control mechanism (Table S3). Remarkably, the magnetic gels demonstrated significantly greater swallowing than the nano-hydrogel. Thus, the larger swallowing might be associated with the increase in hydrophilic groups in the gel matrix present in the surface of the nanoparticles and/or the interaction with the gel network leading to a less dense network [73].

The TEM images of the nanogels containing citrate-stabilized Fe_3O_4 (Figure 4D,E) revealed the presence of rounded particles that display some agglomeration, which might result from the drying process of the samples or nanogels containing clusters of nanoparticles. In addition, both TEM and SEM images suggested that the gels are non-porous (Figures S10 and S11). Taking into account the application of the nanogels in drug delivery, non-porous gels can provide a slower drug release rate [74], which is valuable in obtaining stimuli-responsive systems that enable both the controlled and sustained release of the encapsulated drugs. The measurement of the particles revealed an average size of 22 ± 5 nm for the smaller particles and 112 ± 42 nm for the agglomerates (Figure S10), which indicate that the nanogel network might collapse during the preparation of the samples and thus, resulting in a smaller size than the sizes obtained from DLS. Additionally, the results suggest the existence of nanogels containing clusters of magnetic nanoparticles and/or single nanoparticles. These larger nanogel structures were also observed through SEM (Figure S11). Nonetheless, considering the low polydispersity of the samples in DLS and a strongly negative zeta potential, the aggregation of nanogels is likely to be averted in solution.

3.5. Drug-Loading and Release Assays

The encapsulation of doxorubicin in biopolymer-based nanogels has been demonstrated to be effective in improving the drug half-life owing to the reduction in nanoparticles' clearance and by providing stealth properties [38]. Considering the similarity of the results obtained with both magnetic nanoparticles, the drug loading and release assays were tested for the particles with the best hyperthermia properties, the Fe_3O_4 nanoparticles. The doxorubicin encapsulation efficiencies (EE%) were determined for nano-hydrogels, and magnetic nanogels containing citrate- and BSA-functionalized Fe_3O_4 nanoparticles. As displayed in Figure 5, the encapsulation efficiencies were similar among the nanogels formulations at around 70%, thus indicating that the nanoparticles had little influence on the encapsulation of doxorubicin.

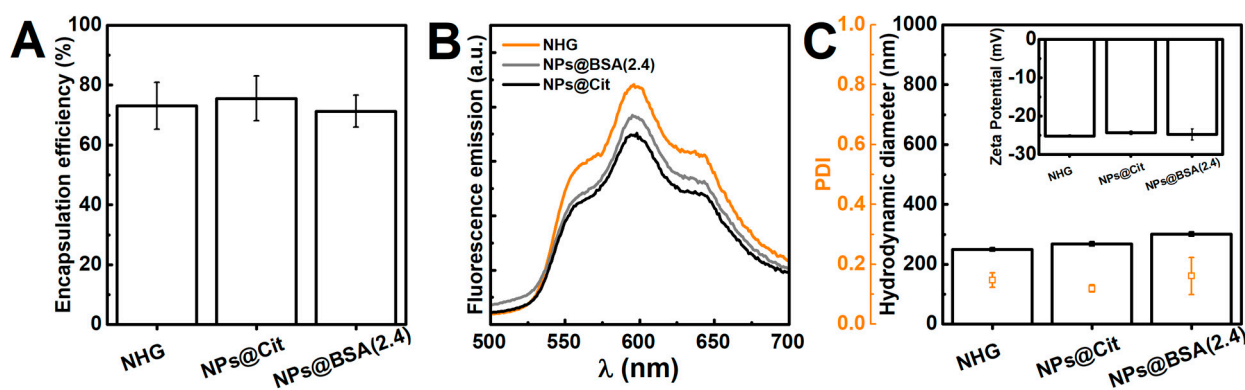


Figure 5. (A) Encapsulation efficiency of doxorubicin in nano-hydrogels (NHG), and magnetic nanogels containing citrate- and BSA-functionalized nanoparticles. The nanogels were initially loaded with doxorubicin for a final concentration of $40 \mu\text{M}$. (B) Fluorescence emission of the doxorubicin loaded nanogels ($\lambda_{480\text{nm}} = 480 \text{ nm}$). (C) Hydrodynamic diameter and polydispersity index (PDI) of the assessed (magnetic) nanogels loaded with doxorubicin. Insets: zeta potential of the doxorubicin loaded (magnetic) nanogels.

The photophysical properties of doxorubicin allowed for the confirmation of its encapsulation in the nanogels. The strong fluorescence emission, the maximum fluorescence wavelength around 595 nm, and the ratio between the intensities at 550 nm (I_1) and 595 nm (I_2) are indicative of the localization of doxorubicin in an environment less polar than water [48,75]. According to the intensity ratios ($I_1/I_2 \sim 0.543 \pm 0.014$) described by Karukstis et al. [75], the polarity is similar to 1-hexanol (dielectric constant, $\epsilon = 13.3$). The shape of the emission band also approaches the doxorubicin spectra described by Cardoso et al. [76] in organic protic solvents, such as ethanol and methanol. A fluorescence emission quenching effect was also observed for the magnetic nanoparticles, which is stronger for the gels containing citrate-stabilized nanoparticles. This effect has been reported for several antitumour drugs encapsulated in magnetic gels [48,77], which is indicative of the close proximity of the drugs to the nanoparticles. Hence, considering the mentioned results, doxorubicin might localize close to the core of the nanogels and establish hydrogen bonds with the hydroxyl groups of the polysaccharide chains. In addition, the encapsulation of doxorubicin did not induce major changes in the hydrodynamic diameter and polydispersity, and as the zeta potential remained mostly unaffected (correlograms in Figure S12), it further suggests doxorubicin localization in the core of the nanogels. Nonetheless, the formation of complexes between doxorubicin and alginate is not excluded. It is also worth noting that the hydrodynamic size of doxorubicin-loaded magnetic nanogels (~ 200 nm) and their zeta potential (~ -25 mV) endow the nanosystem as suitable for intravenous injection [78,79].

The release of doxorubicin from nanogels was carried out at pH = 6 and pH = 7.4 to assess the effect of pH and simulate the acidic conditions in tumor microenvironments and neutral physiological media [80,81], respectively. In addition, the particle functionalization (citrate or BSA) was also evaluated and compared with the release from nanogels. The passive release profiles depicted in Figure 6A,B demonstrated an initial fast release rate of doxorubicin during the first 24 h, which can be associated to the loosely bound doxorubicin on the nanogels. This initial phase was followed by a slower release in the subsequent hours. Similar release profiles have been observed for other types of self-assembled (nano)gels [82–84]. Importantly, the drug is not completely released after 3 days, indicating a strong association between doxorubicin and the nanogel matrix. A comparison of the total drug release at pH = 7.4 and 6 demonstrates a higher release of doxorubicin at lower pH. However, it is worth noting that the observed enhancement in drug release is not strongly different during the initial 24 h. This phenomenon can be attributed to the increased stability of the nanogels' matrix resulting from enhanced electrostatic interactions between alginate and chitosan, which might effectively slow down the release of the drug [85]. Nevertheless, the results are in line with the increased hydrophilicity of doxorubicin at an acidic pH facilitating its release. Additionally, the incorporation of nanoparticles contributed to an improved sustained release of doxorubicin, namely in the gels with BSA-functionalized nanoparticles. This effect can be associated with the additional hydrophilic and hydrophobic contacts provided by BSA [60]. BSA-based nanoparticles have been demonstrated to be a suitable strategy to obtain pH-sensitive systems for the release of doxorubicin [86]. Therefore, the results indicate that the functionalization with BSA provides a suitable strategy to further reduce the release of doxorubicin in physiological pH while guaranteeing an unaffected enhanced release at pH 6. Notably, the release profiles indicate that the developed magnetic nanogels display improved sustained doxorubicin release compared with other reported nanogels based on chitosan and/or alginate [87–89]. In addition, the developed strategy might be adaptable to the encapsulation of proteins with biological functions, such as lactoferrin [90].

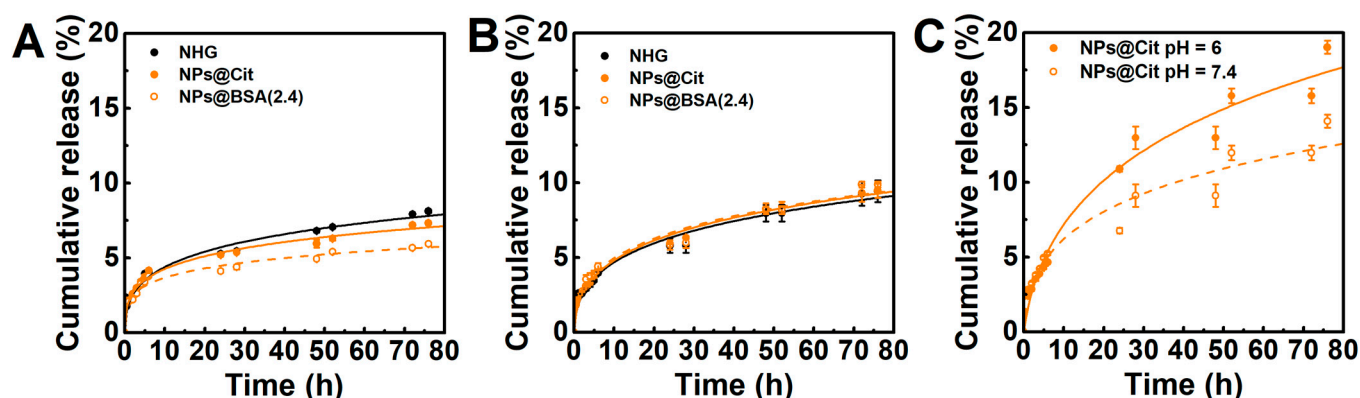


Figure 6. Cumulative doxorubicin release profiles from nano-hydrogels (NHG) and magnetic nanogels containing citrate- and BSA-functionalized nanoparticles at (A) pH = 7.4 and (B) pH = 6, and (C) from magnetic nanogels with citrate-functionalized nanoparticles exposed to 808 nm laser irradiation ($1 \text{ W}/\text{cm}^2$, 10 min after each aliquot). The release profiles were fitted to Gompertz model over the 76 h.

The dose-dependent cardiotoxicity of doxorubicin is a significant limitation, frequently resulting in cardiac atrophy years after the anthracycline exposure, which has been demonstrated in mice to be a dose-dependent effect that begins at relatively low dose exposure [91]. Hence, considering the need for a better control of drug release to minimize the side effects and increase the efficacy of the therapeutic strategy, the nanogels containing citrate-stabilized nanoparticles were evaluated for their ability to release drugs upon laser irradiation. The results showed that irradiation with an 808 nm laser ($1 \text{ W}/\text{cm}^2$) led to a slight enhancement of the release within the initial 24 h, and also enhanced the release during the subsequent slower phase after each irradiation period. Notably, this effect was observed at both pH 7.4 and pH 6, suggesting that the systems are not only pH-responsive but also temperature-responsive. Additionally, in line with the passive release results, active release was also more pronounced at pH 6 compared with pH 7.4. This finding indicates that the effect will be even stronger in proximity to the tumor, as tumors typically exhibit a more acidic pH in their microenvironment. Consequently, drug release can be spatially enhanced and controlled within tumors. Considering that controlled release systems aim to maintain drugs at target sites with therapeutic concentrations, as well as regulate the release rate and duration, the developed magnetic nanogels hold promise as nanosystems for delivering doxorubicin.

The cumulative drug release profiles were subjected to fitting with various mathematical models (Table S4), including the Korsmeyer–Peppas and first-order models [92]. The observed curvilinear nature of the release profiles suggests that the nanoparticles deviate from following a first-order kinetic pattern. Instead, the fitting analysis of the release profiles revealed that the Korsmeyer–Peppas model provide a better description of the results. This model can be applied to systems with different geometries, as long as perfect sink conditions are maintained [92,93]. Furthermore, the Gompertz empirical model also demonstrated a good fit to the data, allowing the comparison of the release kinetics.

The parameter n in the Korsmeyer–Peppas model serves as an indicator of the diffusion mechanism (Table S5). Values of n below 0.5 are associated with a diffusion-controlled release mechanism, which was obtained during the initial 6 h of analysis (Table S6). This further supports the stability of the nanosystems and suggests that a Fickian diffusion process governs the sustained release of doxorubicin. Interestingly, the diffusion mechanism remained unchanged during laser irradiation, with the heating effect originating from the magnetic nanoparticles primarily manifesting as an increase in the rate constant. This observation indicates that the system maintains its stability during irradiation, as the release mechanism remains consistent, and the release is potentially enhanced due to the thermal effects facilitating drug diffusion.

It is also important to note that chitosan/alginate nanogels have been widely reported to be biocompatible and suitable for cancer therapy [79]. For example, Yoncheva et al. [78] developed chitosan/alginate nanogels with an approximate diameter around 300 nm, which displayed a doxorubicin release profile characterized by pH-responsive behavior. The authors reported the nanogels' efficacy against melanoma in in vivo experiments, revealing suitable intracellular accumulation and a prolonged cytotoxic impact on cancer cells. However, composite-based nanogels can provide further improved therapeutic outcomes by enabling the use of dual strategies, such as pH/redox, magnetic/pH, and photothermal responsiveness [38,94]. For instance, Bergueiro et al. [95] developed nanogels composed of a thermoresponsive polymer cross-linked by plasmonic gold nanoparticles, showcasing a temperature-triggered chemotherapy approach that effectively inhibited tumour growth. However, the system displayed a burst release in the initial 6 h, which raised concerns regarding undesired side effects, it and could not be magnetically guided. In contrast, Huang et al. [96] developed GSH/pH co-triggered magnetic nanogels based on thiolated alginate and thiolated magnetic nanoparticles, which was found to have cytocompatibility and also to be effective in inhibiting tumor cell growth. Recent studies have demonstrated the superior photothermia capability of iron oxide nanoparticles compared with magnetic hyperthermia, particularly achieving large heating efficiency at a low dosage of nanoparticles [31,97,98]. Hence, in this work, besides the sustained release and pH-responsiveness achieved with the chitosan/alginate nanogels, the use of the photothermia capability of magnetic nanoparticles can provide a valuable strategy in controlling drug release, as in the case of gold nanoparticles, while enabling the use of magnetic targeting and synergistically enhancing the therapeutic efficacy.

4. Conclusions

In this work, superparamagnetic iron oxide (Fe_3O_4) and manganese ferrite (MnFe_2O_4) nanoparticles with multicore-like morphology and an average physical diameter of 20 ± 3 nm and 11 ± 2 nm were synthesized, respectively. The Fe_3O_4 nanoparticles showed larger saturation magnetization, magnetic hyperthermia, and photothermia (at 808 nm) heating efficiency compared with manganese ferrite nanoparticles. The functionalization of the nanoparticles with citrate and bovine serum albumin (BSA) resulted in changes in their hydrodynamic properties and stability, and both could be formulated into nanogels based on chitosan and alginate using a self-assembly method. The obtained magnetic nanogels were negatively charged (~ -25 mV), with hydrodynamic diameters in the 200–300 nm range, and displayed a similar doxorubicin encapsulation efficiency, which was determined to be around 70%. The release of doxorubicin from the nanogels exhibited a sustained release profile, driven by a diffusion-controlled mechanism. The incorporation of nanoparticles, namely those functionalized with BSA, improved the sustained release at physiological pH. Additionally, the acidic pH and photothermia effect enhanced the release of doxorubicin from the magnetic nanogels. Overall, the developed magnetic nanogels displayed promising results for controlled and enhanced drug delivery, with potential applications in cancer therapy.

Supplementary Materials: The following supporting information can be downloaded at: <https://www.mdpi.com/article/10.3390/pharmaceutics15092194/s1>, Figure S1: TEM images of nanoparticles; Figure S2: UV-vis spectra of nanoparticles; Table S1: Magnetic properties of nanoparticles; Figure S3: DLS results of nanoparticles; Table S2: Hydrodynamic properties of nanoparticles; Figure S4: Urbach plots of the nanoparticles; Figure S5: Heating profiles obtained from magnetic hyperthermia; Figure S6: DLS results of functionalized nanoparticles; Figure S7: UV-vis results of functionalized nanoparticles; Figure S8: DLS results of nanogels; Figure S9: Swelling kinetics of nanogels; Figure S10: TEM results of nanogels; Figure S11: SEM images of nanogels; Figure S12: DLS results of magnetic nanogels loaded with doxorubicin; Table S3: Parameters obtained from the fitting of Korsmeyer–Peppas and second-order swelling kinetics models to the swelling curves; Table S4: Coefficients of determination of several models fitted to release profiles; Table S5: Release coefficients obtained for the Korsmeyer–Peppas and Gompertz models fitted to the release profiles.

Author Contributions: Conceptualization, S.R.S.V. and E.M.S.C.; methodology, S.R.S.V., P.V.R., C.M. and C.O.A.; validation, C.M., V.S.A., M.A.C.-D. and E.M.S.C.; formal analysis, S.R.S.V., E.S.M. and C.O.A.; investigation, S.R.S.V., E.S.M., P.V.R. and C.O.A.; writing—original draft preparation, S.R.S.V.; writing—review and editing, E.M.S.C.; visualization, C.M., V.S.A. and M.A.C.-D.; supervision, V.S.A., M.A.C.-D. and E.M.S.C.; project administration, M.A.C.-D. All authors have read and agreed to the published version of the manuscript.

Funding: This work was funded by the Portuguese Foundation for Science and Technology (FCT) in the framework of the Strategic Funding of CF-UM-UP (UIDB/04650/2020), and by the Ministerio de Economía y Competitividad de España (PID2020-113704RB-I00 and PID2020-119242RB-I00), Xunta de Galicia (Centro Singular de Investigación de Galicia—Accreditation 2019-2022 ED431G 2019/06 and IN607A 2018/5 and project ED431C 2020-06), the European Union (EU-ERDF Interreg V-A—Spain-Portugal 0245_IBEROS_1_E, 0712_ACUINANO_1_E, and 0624_2IQBIONEURO_6_E, and Interreg Atlantic Area NANOCULTURE 1.102.531), and the European Union H2020-MSCA-RISE-2019 PEPSA-MATE project. S.R.S. Veloso acknowledges FCT for a PhD grant (SFRH/BD/144017/2019). Support from MAP-Fis Doctoral Programme is also acknowledged.

Institutional Review Board Statement: Not applicable.

Informed Consent Statement: Not applicable.

Data Availability Statement: The data presented in this study are available in this article (and Supplementary Materials).

Conflicts of Interest: The authors declare no conflict of interest.

References

1. Wang, H.; Deng, H.; Gao, M.; Zhang, W. Self-Assembled Nanogels Based on Ionic Gelation of Natural Polysaccharides for Drug Delivery. *Front. Bioeng. Biotechnol.* **2021**, *9*, 703559. [[CrossRef](#)] [[PubMed](#)]
2. Wang, Y.; Xu, S.; Xiong, W.; Pei, Y.; Li, B.; Chen, Y. Nanogels Fabricated from Bovine Serum Albumin and Chitosan via Self-Assembly for Delivery of Anticancer Drug. *Colloids Surf. B Biointerfaces* **2016**, *146*, 107–113. [[CrossRef](#)]
3. Nahi, O.; Kulak, A.N.; Kress, T.; Kim, Y.-Y.; Grendal, O.G.; Duer, M.J.; Cayre, O.J.; Meldrum, F.C. Incorporation of Nanogels within Calcite Single Crystals for the Storage, Protection and Controlled Release of Active Compounds. *Chem. Sci.* **2021**, *12*, 9839–9850. [[CrossRef](#)] [[PubMed](#)]
4. Zhang, Y.; Zhang, D.; Wang, J.-T.; Zhang, X.; Yang, Y. Fabrication of Stimuli-Responsive Nanogels for Protein Encapsulation and Traceless Release without Introducing Organic Solvents, Surfactants, or Small-Molecule Cross-Linkers. *Polym. Chem.* **2021**, *12*, 554–563. [[CrossRef](#)]
5. Abedi, F.; Ghandforoushan, P.; Adeli, F.; Yousefnezhad, M.; Mohammadi, A.; Moghaddam, S.V.; Davaran, S. Development of Stimuli-Responsive Nanogels as Drug Carriers and Their Biomedical Application in 3D Printing. *Mater. Today Chem.* **2023**, *29*, 101372. [[CrossRef](#)]
6. Schütz, C.A.; Juillerat-Jeanneret, L.; Käuper, P.; Wandrey, C. Cell Response to the Exposure to Chitosan-TPP//Alginate Nanogels. *Biomacromolecules* **2011**, *12*, 4153–4161. [[CrossRef](#)]
7. El-Feky, G.S.; El-Banna, S.T.; El-Bahy, G.S.; Abdelrazek, E.M.; Kamal, M. Alginate Coated Chitosan Nanogel for the Controlled Topical Delivery of Silver Sulfadiazine. *Carbohydr. Polym.* **2017**, *177*, 194–202. [[CrossRef](#)] [[PubMed](#)]
8. Son, Y. Biodistribution and Anti-Tumor Efficacy of Doxorubicin Loaded Glycol-Chitosan Nanoaggregates by EPR Effect. *J. Control. Release* **2003**, *91*, 135–145. [[CrossRef](#)]
9. Aslzad, S.; Heydari, P.; Abdolahinia, E.D.; Amiryaghoubi, N.; Safary, A.; Fathi, M.; Erfan-Niya, H. Chitosan/Gelatin Hybrid Nanogel Containing Doxorubicin as Enzyme-Responsive Drug Delivery System for Breast Cancer Treatment. *Colloid Polym. Sci.* **2023**, *301*, 273–281. [[CrossRef](#)]
10. Akram, M.U.; Abbas, N.; Farman, M.; Manzoor, S.; Khan, M.I.; Osman, S.M.; Luque, R.; Shanableh, A. Tumor Micro-Environment Sensitive Release of Doxorubicin through Chitosan Based Polymeric Nanoparticles: An In-Vitro Study. *Chemosphere* **2023**, *313*, 137332. [[CrossRef](#)] [[PubMed](#)]
11. Heragh, B.K.; Taherinezhad, H.; Mahdavinia, G.R.; Javanshir, S.; Labib, P.; Ghasemsolb, S. PH-Responsive Co-Delivery of Doxorubicin and Saffron via Cross-Linked Chitosan/Laponite RD Nanoparticles for Enhanced-Chemotherapy. *Mater. Today Commun.* **2023**, *34*, 104956. [[CrossRef](#)]
12. Ashrafizadeh, M.; Hushmandi, K.; Mirzaei, S.; Bokaie, S.; Bigham, A.; Makvandi, P.; Rabiee, N.; Thakur, V.K.; Kumar, A.P.; Sharifi, E.; et al. Chitosan-based Nanoscale Systems for Doxorubicin Delivery: Exploring Biomedical Application in Cancer Therapy. *Bioeng. Transl. Med.* **2023**, *8*, e10325. [[CrossRef](#)] [[PubMed](#)]
13. Zhou, Y.; Li, S.; Tan, W.; Wei, X.; Chang, Y.; Yi, Q.; Pu, C.; Wang, J. Design, Synthesis, and Preparation of Ultrasound-Responsive Curcumin-Loaded Chitosan Nanocarriers. *Russ. J. Gen. Chem.* **2023**, *93*, 108–115. [[CrossRef](#)]

14. Xue, J.; Luo, Y. Protein-Polysaccharide Nanocomplexes as Nanocarriers for Delivery of Curcumin: A Comprehensive Review on Preparation Methods and Encapsulation Mechanisms. *J. Future Foods* **2023**, *3*, 99–114. [[CrossRef](#)]
15. Rajaei, M.; Rashedi, H.; Yazdian, F.; Navaei-Nigjeh, M.; Rahdar, A.; Díez-Pascual, A.M. Chitosan/Agarose/Graphene Oxide Nanohydrogel as Drug Delivery System of 5-Fluorouracil in Breast Cancer Therapy. *J. Drug Deliv. Sci. Technol.* **2023**, *82*, 104307. [[CrossRef](#)]
16. Smitha, K.T.; Anitha, A.; Furuike, T.; Tamura, H.; Nair, S.V.; Jayakumar, R. In Vitro Evaluation of Paclitaxel Loaded Amorphous Chitin Nanoparticles for Colon Cancer Drug Delivery. *Colloids Surf. B Biointerfaces* **2013**, *104*, 245–253. [[CrossRef](#)] [[PubMed](#)]
17. Nalini, T.; Basha, S.K.; Sadiq, A.M.; Kumari, V.S. In Vitro Cytocompatibility Assessment and Antibacterial Effects of Quercetin Encapsulated Alginate/Chitosan Nanoparticle. *Int. J. Biol. Macromol.* **2022**, *219*, 304–311. [[CrossRef](#)] [[PubMed](#)]
18. Hesani, M.; Gholipour-Kanani, A.; Lotfi, M.; Shafiee, M. The Synthesis and Characterization of Core-Shell Nanogels Based on Alginate and Chitosan for the Controlled Delivery of Mupirocin. *Biochem. Eng. J.* **2023**, *190*, 108742. [[CrossRef](#)]
19. Thai, H.; Thuy Nguyen, C.; Thi Thach, L.; Thi Tran, M.; Duc Mai, H.; Thi Thu Nguyen, T.; Duc Le, G.; Van Can, M.; Dai Tran, L.; Long Bach, G.; et al. Characterization of Chitosan/Alginate/Lovastatin Nanoparticles and Investigation of Their Toxic Effects In Vitro and In Vivo. *Sci. Rep.* **2020**, *10*, 909. [[CrossRef](#)] [[PubMed](#)]
20. Aires, A.; Ocampo, S.M.; Cabrera, D.; de la Cueva, L.; Salas, G.; Teran, F.J.; Cortajarena, A.L. BSA-Coated Magnetic Nanoparticles for Improved Therapeutic Properties. *J. Mater. Chem. B* **2015**, *3*, 6239–6247. [[CrossRef](#)]
21. Li, Z.; Qiang, L.; Zhong, S.; Wang, H.; Cui, X. Synthesis and Characterization of Monodisperse Magnetic Fe₃O₄@BSA Core-Shell Nanoparticles. *Colloids Surf. A Physicochem. Eng. Asp.* **2013**, *436*, 1145–1151. [[CrossRef](#)]
22. Novikau, I.S.; Novak, E.V.; Pyanzina, E.S.; Kantorovich, S.S. Behaviour of a Magnetic Nanogel in a Shear Flow. *J. Mol. Liq.* **2022**, *346*, 118056. [[CrossRef](#)]
23. Sung, B.; Kim, M.; Abelmann, L. Magnetic Microgels and Nanogels: Physical Mechanisms and Biomedical Applications. *Bioeng. Transl. Med.* **2021**, *6*, e10190. [[CrossRef](#)]
24. Demarchi, C.A.; Debrassi, A.; de Campos Buzzi, F.; Corrêa, R.; Filho, V.C.; Rodrigues, C.A.; Nedelko, N.; Demchenko, P.; Ślowska-Waniewska, A.; Dłużewski, P.; et al. A Magnetic Nanogel Based on O-Carboxymethylchitosan for Antitumor Drug Delivery: Synthesis, Characterization and in Vitro Drug Release. *Soft Matter* **2014**, *10*, 3441–3450. [[CrossRef](#)] [[PubMed](#)]
25. Chow, J.C.L. Magnetic Nanoparticles as Contrast Agents in Magnetic Resonance Imaging and Radiosensitizers in Radiotherapy. In *Fundamentals and Industrial Applications of Magnetic Nanoparticles*; Woodhead Publishing Series in Electronic and Optical Materials; Elsevier: Amsterdam, The Netherlands, 2022; pp. 291–316. [[CrossRef](#)]
26. Wang, S.; Hou, Y. Photothermal Therapy Based on Magnetic Nanoparticles in Cancer. *J. Appl. Phys.* **2021**, *130*, 070902. [[CrossRef](#)]
27. Estelrich, J.; Busquets, M. Iron Oxide Nanoparticles in Photothermal Therapy. *Molecules* **2018**, *23*, 1567. [[CrossRef](#)]
28. Wu, H.; Liu, L.; Song, L.; Ma, M.; Gu, N.; Zhang, Y. Enhanced Tumor Synergistic Therapy by Injectable Magnetic Hydrogel Mediated Generation of Hyperthermia and Highly Toxic Reactive Oxygen Species. *ACS Nano* **2019**, *13*, 14013–14023. [[CrossRef](#)] [[PubMed](#)]
29. Tzoneva, R.; Tsiapla, A.-R.; Uzunova, V.; Stoyanova, T.; Samaras, T.; Angelakeris, M.; Kalogirou, O. Synergistic Effect of Combined Treatment with Magnetic Hyperthermia and Magneto-Mechanical Stress of Breast Cancer Cells. *Magnetochemistry* **2022**, *8*, 117. [[CrossRef](#)]
30. Chu, M.; Shao, Y.; Peng, J.; Dai, X.; Li, H.; Wu, Q.; Shi, D. Near-Infrared Laser Light Mediated Cancer Therapy by Photothermal Effect of Fe₃O₄ Magnetic Nanoparticles. *Biomaterials* **2013**, *34*, 4078–4088. [[CrossRef](#)]
31. Nemes, S.; Kralj, S.; Wilhelm, C.; Abou-Hassan, A.; Rols, M.-P.; Kolosnjaj-Tabi, J. Comparison of Iron Oxide Nanoparticles in Photothermal and Magnetic Hyperthermia: Effects of Clustering and Silica Encapsulation on Nanoparticles' Heating Yield. *Appl. Sci.* **2020**, *10*, 7322. [[CrossRef](#)]
32. Li, C.; Obireddy, S.R.; Lai, W.-F. Preparation and Use of Nanogels as Carriers of Drugs. *Drug Deliv.* **2021**, *28*, 1594–1602. [[CrossRef](#)]
33. Soni, K.S.; Desale, S.S.; Bronich, T.K. Nanogels: An Overview of Properties, Biomedical Applications and Obstacles to Clinical Translation. *J. Control. Release* **2016**, *240*, 109–126. [[CrossRef](#)] [[PubMed](#)]
34. de Lima, C.S.A.; Balogh, T.S.; Varca, J.P.R.O.; Varca, G.H.C.; Lugão, A.B.; Camacho-Cruz, L.A.; Bucio, E.; Kadlubowski, S.S. An Updated Review of Macro, Micro, and Nanostructured Hydrogels for Biomedical and Pharmaceutical Applications. *Pharmaceutics* **2020**, *12*, 970. [[CrossRef](#)]
35. Pamfil, D.; Vasile, C. Nanogels of Natural Polymers. In *Polymer Gels. Gels Horizons: From Science to Smart Materials*; Thakur, V., Thakur, M., Voicu, S., Eds.; Springer: Singapore, 2018; pp. 71–110.
36. Liao, J.; Huang, H. Review on Magnetic Natural Polymer Constructed Hydrogels as Vehicles for Drug Delivery. *Biomacromolecules* **2020**, *21*, 2574–2594. [[CrossRef](#)] [[PubMed](#)]
37. Gallo, E.; Diaferia, C.; Rosa, E.; Smaldone, G.; Morelli, G.; Accardo, A. Peptide-Based Hydrogels and Nanogels for Delivery of Doxorubicin. *Int. J. Nanomed.* **2021**, *16*, 1617–1630. [[CrossRef](#)]
38. Mohammadi, M.; Arabi, L.; Alibolandi, M. Doxorubicin-Loaded Composite Nanogels for Cancer Treatment. *J. Control. Release* **2020**, *328*, 171–191. [[CrossRef](#)] [[PubMed](#)]
39. Mohammadi, M.; Taghavi, S.; Abnous, K.; Taghdisi, S.M.; Ramezani, M.; Alibolandi, M. Hybrid Vesicular Drug Delivery Systems for Cancer Therapeutics. *Adv. Funct. Mater.* **2018**, *28*, 1802136. [[CrossRef](#)]

40. Bertuit, E.; Benassai, E.; Méridet, G.; Greneche, J.-M.; Baptiste, B.; Neveu, S.; Wilhelm, C.; Abou-Hassan, A. Structure–Property–Function Relationships of Iron Oxide Multicore Nanoflowers in Magnetic Hyperthermia and Photothermia. *ACS Nano* **2022**, *16*, 271–284. [[CrossRef](#)] [[PubMed](#)]
41. Cabana, S.; Curcio, A.; Michel, A.; Wilhelm, C.; Abou-Hassan, A. Iron Oxide Mediated Photothermal Therapy in the Second Biological Window: A Comparative Study between Magnetite/Maghemite Nanospheres and Nanoflowers. *Nanomaterials* **2020**, *10*, 1548. [[CrossRef](#)] [[PubMed](#)]
42. Hugouenq, P.; Levy, M.; Alloyeau, D.; Lartigue, L.; Dubois, E.; Cabuil, V.; Ricolleau, C.; Roux, S.; Wilhelm, C.; Gazeau, F.; et al. Iron Oxide Monocrystalline Nanoflowers for Highly Efficient Magnetic Hyperthermia. *J. Phys. Chem. C* **2012**, *116*, 15702–15712. [[CrossRef](#)]
43. Andrade, R.G.D.; Ferreira, D.; Veloso, S.R.S.; Santos-Pereira, C.; Castanheira, E.M.S.; Côte-Real, M.; Rodrigues, L.R. Synthesis and Cytotoxicity Assessment of Citrate-Coated Calcium and Manganese Ferrite Nanoparticles for Magnetic Hyperthermia. *Pharmaceutics* **2022**, *14*, 2694. [[CrossRef](#)] [[PubMed](#)]
44. Amorim, C.O.; Mohseni, F.; Dumas, R.K.; Amaral, V.S.; Amaral, J.S. A Geometry-Independent Moment Correction Method for the MPMS3 SQUID-Based Magnetometer. *Meas. Sci. Technol.* **2021**, *32*, 105602. [[CrossRef](#)]
45. Plan Sangnier, A.; Preveral, S.; Curcio, A.; Silva, A.K.; Lefèvre, C.T.; Pignol, D.; Lalatonne, Y.; Wilhelm, C. Targeted Thermal Therapy with Genetically Engineered Magnetite Magnetosomes@RGD: Photothermia Is Far More Efficient than Magnetic Hyperthermia. *J. Control. Release* **2018**, *279*, 271–281. [[CrossRef](#)]
46. Beji, Z.; Sun, M.; Smiri, L.S.; Herbst, F.; Mangeney, C.; Ammar, S. Polyol Synthesis of Non-Stoichiometric Mn–Zn Ferrite Nanocrystals: Structural /Microstructural Characterization and Catalytic Application. *RSC Adv.* **2015**, *5*, 65010–65022. [[CrossRef](#)]
47. Hemery, G.; Keyes, A.C.; Garaio, E.; Rodrigo, I.; Garcia, J.A.; Plazaola, F.; Garanger, E.; Sandre, O. Tuning Sizes, Morphologies, and Magnetic Properties of Monocore Versus Multicore Iron Oxide Nanoparticles through the Controlled Addition of Water in the Polyol Synthesis. *Inorg. Chem.* **2017**, *56*, 8232–8243. [[CrossRef](#)]
48. Veloso, S.R.S.; Silva, J.F.G.; Hilliou, L.; Moura, C.; Coutinho, P.J.G.; Martins, J.A.; Testa-Anta, M.; Salgueiriño, V.; Correa-Duarte, M.A.; Ferreira, P.M.T.; et al. Impact of Citrate and Lipid-Functionalized Magnetic Nanoparticles in Dehydropeptide Supramolecular Magnetogels: Properties, Design and Drug Release. *Nanomaterials* **2021**, *11*, 16. [[CrossRef](#)]
49. Gholizadeh, A. A Comparative Study of Physical Properties in Fe₃O₄ Nanoparticles Prepared by Coprecipitation and Citrate Methods. *J. Am. Ceram. Soc.* **2017**, *100*, 3577–3588. [[CrossRef](#)]
50. Veloso, S.R.S.; Andrade, R.G.D.; Gomes, V.; Amorim, C.O.; Amaral, V.S.; Salgueiriño, V.; Coutinho, P.J.G.; Ferreira, P.M.T.; Correa-Duarte, M.A.; Castanheira, E.M.S. Oxidative Precipitation Synthesis of Calcium-Doped Manganese Ferrite Nanoparticles for Magnetic Hyperthermia. *Int. J. Mol. Sci.* **2022**, *23*, 14145. [[CrossRef](#)]
51. Dippong, T.; Levei, E.A.; Deac, I.G.; Petean, I.; Cadar, O. Dependence of Structural, Morphological and Magnetic Properties of Manganese Ferrite on Ni-Mn Substitution. *Int. J. Mol. Sci.* **2022**, *23*, 3097. [[CrossRef](#)]
52. Ahmad, S.; Ali, S.; Ullah, I.; Zobaer, M.S.; Albakri, A.; Muhammad, T. Synthesis and Characterization of Manganese Ferrite from Low Grade Manganese Ore through Solid State Reaction Route. *Sci. Rep.* **2021**, *11*, 16190. [[CrossRef](#)]
53. Tang, J.; Myers, M.; Bosnick, K.A.; Brus, L.E. Magnetite Fe₃O₄ Nanocrystals: Spectroscopic Observation of Aqueous Oxidation Kinetics. *J. Phys. Chem. B* **2003**, *107*, 7501–7506. [[CrossRef](#)]
54. Caruntu, D.; Caruntu, G.; O'Connor, C.J. Magnetic Properties of Variable-Sized Fe₃O₄ Nanoparticles Synthesized from Non-Aqueous Homogeneous Solutions of Polyols. *J. Phys. D: Appl. Phys.* **2007**, *40*, 5801–5809. [[CrossRef](#)]
55. Lozano-Pedraza, C.; Plaza-Mayoral, E.; Espinosa, A.; Sot, B.; Serrano, A.; Salas, G.; Blanco-Andujar, C.; Cotin, G.; Felder-Flesch, D.; Begin-Colin, S.; et al. Assessing the Parameters Modulating Optical Losses of Iron Oxide Nanoparticles under near Infrared Irradiation. *Nanoscale Adv.* **2021**, *3*, 6490–6502. [[CrossRef](#)] [[PubMed](#)]
56. Freis, B.; Ramirez, M.D.L.A.; Kiefer, C.; Harlepp, S.; Iacovita, C.; Henoumont, C.; Affolter-Zbarszczuk, C.; Meyer, F.; Mertz, D.; Boos, A.; et al. Effect of the Size and Shape of Dendronized Iron Oxide Nanoparticles Bearing a Targeting Ligand on MRI, Magnetic Hyperthermia, and Photothermia Properties—From Suspension to In Vitro Studies. *Pharmaceutics* **2023**, *15*, 1104. [[CrossRef](#)] [[PubMed](#)]
57. Kolokithas-Ntoukas, A.; Bakandritsos, A.; Belza, J.; Kesa, P.; Herynek, V.; Pankrac, J.; Angelopoulou, A.; Malina, O.; Avgoustakis, K.; Georgakilas, V.; et al. Condensed Clustered Iron Oxides for Ultrahigh Photothermal Conversion and In Vivo Multimodal Imaging. *ACS Appl. Mater. Interfaces* **2021**, *13*, 29247–29256. [[CrossRef](#)] [[PubMed](#)]
58. Barik, A.; Priyadarsini, K.I.; Mohan, H. Photophysical Studies on Binding of Curcumin to Bovine Serum Albumin. *Photochem. Photobiol.* **2007**, *77*, 597–603. [[CrossRef](#)]
59. Bronze-Uhle, E.; Costa, B.C.; Ximenes, V.F.; Lisboa-Filho, P.N. Synthetic Nanoparticles of Bovine Serum Albumin with Entrapped Salicylic Acid. *Nanotechnol. Sci. Appl.* **2016**, *10*, 11–21. [[CrossRef](#)]
60. Agudelo, D.; Bourassa, P.; Bruneau, J.; Bérubé, G.; Asselin, É.; Tajmir-Riahi, H.-A. Probing the Binding Sites of Antibiotic Drugs Doxorubicin and N-(Trifluoroacetyl) Doxorubicin with Human and Bovine Serum Albumins. *PLoS ONE* **2012**, *7*, e43814. [[CrossRef](#)]
61. Hernández-Arteaga, A.C.; Delgado-Nieblas, F.C.; Ojeda-Galván, H.J.; Velázquez-Salazar, J.J.; Vinogradova, E.; José-Yacamán, M.; Guirado-López, R.A.; Navarro-Contreras, H.R. Surface-Enhanced Raman Spectroscopy of Acetyl-Neuraminic Acid on Silver Nanoparticles: Role of the Passivating Agent on the Adsorption Efficiency and Amplification of the Raman Signal. *J. Phys. Chem. C* **2017**, *121*, 21045–21056. [[CrossRef](#)]

62. Huang, Z.; Chen, X.; Li, Y.; Chen, J.; Lin, J.; Wang, J.; Lei, J.; Chen, R. Quantitative Determination of Citric Acid in Seminal Plasma by Using Raman Spectroscopy. *Appl. Spectrosc.* **2013**, *67*, 757–760. [[CrossRef](#)]
63. Pandoli, O.; Martins, R.D.S.; Romani, E.C.; Paciornik, S.; Maurício, M.H.D.P.; Alves, H.D.L.; Pereira-Meirelles, F.V.; Luz, E.L.; Koller, S.M.L.; Valiente, H.; et al. Colloidal Silver Nanoparticles: An Effective Nano-Filler Material to Prevent Fungal Proliferation in Bamboo. *RSC Adv.* **2016**, *6*, 98325–98336. [[CrossRef](#)]
64. Grys, D.-B.; de Nijs, B.; Salmon, A.R.; Huang, J.; Wang, W.; Chen, W.-H.; Scherman, O.A.; Baumberg, J.J. Citrate Coordination and Bridging of Gold Nanoparticles: The Role of Gold Adatoms in AuNP Aging. *ACS Nano* **2020**, *14*, 8689–8696. [[CrossRef](#)] [[PubMed](#)]
65. de Melo, V.H.S.; Zamarion, V.M.; Araki, K.; Toma, H.E. New Insights on Surface-Enhanced Raman Scattering Based on Controlled Aggregation and Spectroscopic Studies, DFT Calculations and Symmetry Analysis for 3,6-Bi-2-Pyridyl-1,2,4,5-Tetrazine Adsorbed onto Citrate-Stabilized Gold Nanoparticles. *J. Raman Spectrosc.* **2011**, *42*, 644–652. [[CrossRef](#)]
66. Fazio, B.; D’Andrea, C.; Foti, A.; Messina, E.; Irrera, A.; Donato, M.G.; Villari, V.; Micali, N.; Maragò, O.M.; Gucciardi, P.G. SERS Detection of Biomolecules at Physiological PH via Aggregation of Gold Nanorods Mediated by Optical Forces and Plasmonic Heating. *Sci. Rep.* **2016**, *6*, 26952. [[CrossRef](#)]
67. Esmonde-White, K.A.; Mandair, G.S.; Raaij, F.; Roessler, B.J.; Morris, M.D. Raman Spectroscopy of Dried Synovial Fluid Droplets as a Rapid Diagnostic for Knee Joint Damage. In *Biomedical Optical Spectroscopy*; Mahadevan-Jansen, A., Petrich, W., Alfano, R.R., Katz, A., Eds.; SPIE: Bellingham, WA, USA, 2008; p. 68530Y.
68. Danaei, M.; Dehghankhold, M.; Ataie, S.; Hasanzadeh Davarani, F.; Javanmard, R.; Dokhani, A.; Khorasani, S.; Mozafari, M.R. Impact of Particle Size and Polydispersity Index on the Clinical Applications of Lipidic Nanocarrier Systems. *Pharmaceutics* **2018**, *10*, 57. [[CrossRef](#)] [[PubMed](#)]
69. Zajac, A.; Hanuza, J.; Wandas, M.; Dymińska, L. Determination of N-Acetylation Degree in Chitosan Using Raman Spectroscopy. *Spectrochim. Acta Part A Mol. Biomol. Spectrosc.* **2015**, *134*, 114–120. [[CrossRef](#)]
70. Campos-Vallette, M.M.; Chandía, N.P.; Clavijo, E.; Leal, D.; Matsuhira, B.; Osorio-Román, I.O.; Torres, S. Characterization of Sodium Alginate and Its Block Fractions by Surface-Enhanced Raman Spectroscopy. *J. Raman Spectrosc.* **2010**, *41*, 758–763. [[CrossRef](#)]
71. Schmid, T.; Messmer, A.; Yeo, B.-S.; Zhang, W.; Zenobi, R. Towards Chemical Analysis of Nanostructures in Biofilms II: Tip-Enhanced Raman Spectroscopy of Alginates. *Anal. Bioanal. Chem.* **2008**, *391*, 1907–1916. [[CrossRef](#)]
72. Yavari, N.; Azizian, S. Mixed Diffusion and Relaxation Kinetics Model for Hydrogels Swelling. *J. Mol. Liq.* **2022**, *363*, 119861. [[CrossRef](#)]
73. Bonhome-Espinosa, A.B.; Campos, F.; Rodriguez, I.A.; Carriel, V.; Marins, J.A.; Zubarev, A.; Duran, J.D.G.; Lopez-Lopez, M.T. Effect of Particle Concentration on the Microstructural and Macromechanical Properties of Biocompatible Magnetic Hydrogels. *Soft Matter* **2017**, *13*, 2928–2941. [[CrossRef](#)]
74. Hafezi Moghaddam, R.; Dadfarnia, S.; Shabani, A.M.H.; Moghaddam, Z.H.; Tavakol, M. Electron Beam Irradiation Synthesis of Porous and Non-Porous Pectin Based Hydrogels for a Tetracycline Drug Delivery System. *Mater. Sci. Eng. C* **2019**, *102*, 391–404. [[CrossRef](#)]
75. Karukstis, K.K.; Thompson, E.H.; Whiles, J.A.; Rosenfeld, R.J. Deciphering the Fluorescence Signature of Daunomycin and Doxorubicin. *Biophys. Chem.* **1998**, *73*, 249–263. [[CrossRef](#)]
76. Cardoso, B.D.; Rodrigues, A.R.O.; Bañobre-López, M.; Almeida, B.G.; Amorim, C.O.; Amaral, V.S.; Coutinho, P.J.G.; Castanheira, E.M.S. Magnetoliposomes Based on Shape Anisotropic Calcium/Magnesium Ferrite Nanoparticles as Nanocarriers for Doxorubicin. *Pharmaceutics* **2021**, *13*, 1248. [[CrossRef](#)]
77. Veloso, S.R.S.; Magalhães, C.A.B.; Rodrigues, A.R.O.; Vilaça, H.; Queiroz, M.-J.R.P.J.; Martins, J.A.; Coutinho, P.J.G.; Ferreira, P.M.T.; Castanheira, E.M.S. Novel Dehydropeptide-Based Magnetogels Containing Manganese Ferrite Nanoparticles as Antitumor Drug Nanocarriers. *Phys. Chem. Chem. Phys.* **2019**, *21*, 10377–10390. [[CrossRef](#)]
78. Yoncheva, K.; Merino, M.; Shenol, A.; Daskalov, N.T.; St. Petkov, P.; Vayssilov, G.N.; Garrido, M.J. Optimization and In-Vitro/in-Vivo Evaluation of Doxorubicin-Loaded Chitosan-Alginate Nanoparticles Using a Melanoma Mouse Model. *Int. J. Pharm.* **2019**, *556*, 1–8. [[CrossRef](#)]
79. Niculescu, A.-G.; Grumezescu, A.M. Applications of Chitosan-Alginate-Based Nanoparticles—An Up-to-Date Review. *Nanomaterials* **2022**, *12*, 186. [[CrossRef](#)] [[PubMed](#)]
80. Huber, V.; Camisaschi, C.; Berzi, A.; Ferro, S.; Lugini, L.; Triulzi, T.; Tuccitto, A.; Tagliabue, E.; Castelli, C.; Rivoltini, L. Cancer Acidity: An Ultimate Frontier of Tumor Immune Escape and a Novel Target of Immunomodulation. *Semin. Cancer Biol.* **2017**, *43*, 74–89. [[CrossRef](#)] [[PubMed](#)]
81. Hao, G.; Xu, Z.P.; Li, L. Manipulating Extracellular Tumour PH: An Effective Target for Cancer Therapy. *RSC Adv.* **2018**, *8*, 22182–22192. [[CrossRef](#)]
82. Veloso, S.R.S.S.; Tiryaki, E.; Spuch, C.; Hilliou, L.; de Oliveira Amorim, C.; Amaral, V.S.; Coutinho, P.J.G.; Ferreira, P.M.T.M.; Salgueiriño, V.V.; Correa-Duarte, M.A.; et al. Tuning the Drug Multimodal Release through a Co-Assembly Strategy Based on Magnetic Gels. *Nanoscale* **2022**, *14*, 5488–5500. [[CrossRef](#)]
83. Wang, Q.-S.; Gao, L.-N.; Zhu, X.-N.; Zhang, Y.; Zhang, C.-N.; Xu, D.; Cui, Y.-L. Co-Delivery of Glycyrrhizin and Doxorubicin by Alginate Nanogel Particles Attenuates the Activation of Macrophage and Enhances the Therapeutic Efficacy for Hepatocellular Carcinoma. *Theranostics* **2019**, *9*, 6239–6255. [[CrossRef](#)] [[PubMed](#)]

84. Elbially, N.S.; Mohamed, N. Alginate-Coated Caseinate Nanoparticles for Doxorubicin Delivery: Preparation, Characterisation, and in Vivo Assessment. *Int. J. Biol. Macromol.* **2020**, *154*, 114–122. [[CrossRef](#)] [[PubMed](#)]
85. Zhang, H.; Xue, Q.; Zhou, Z.; He, N.; Li, S.; Zhao, C. Co-Delivery of Doxorubicin and Hydroxychloroquine via Chitosan/Alginate Nanoparticles for Blocking Autophagy and Enhancing Chemotherapy in Breast Cancer Therapy. *Front. Pharmacol.* **2023**, *14*, 1176232. [[CrossRef](#)]
86. Yang, Z.; Zhang, N.; Ma, T.; Liu, L.; Zhao, L.; Xie, H. Engineered Bovine Serum Albumin-Based Nanoparticles with PH-Sensitivity for Doxorubicin Delivery and Controlled Release. *Drug Deliv.* **2020**, *27*, 1156–1164. [[CrossRef](#)]
87. Sahatsapan, N.; Rojanarata, T.; Ngawhirunpat, T.; Opanasopit, P.; Patrojanasophon, P. Doxorubicin-Loaded Chitosan-Alginate Nanoparticles with Dual Mucoadhesive Functionalities for Intravesical Chemotherapy. *J. Drug Deliv. Sci. Technol.* **2021**, *63*, 102481. [[CrossRef](#)]
88. Yang, L.; Ling, J.; Wang, N.; Jiang, Y.; Lu, Y.; Yang, L.-Y.; Ouyang, X. Delivery of Doxorubicin by Dual Responsive Carboxymethyl Chitosan Based Nanogel and in Vitro Performance. *Mater. Today Commun.* **2022**, *31*, 103781. [[CrossRef](#)]
89. Alioghli Ziaei, A.; Erfan-Niya, H.; Fathi, M.; Amiraghoubi, N. In Situ Forming Alginate/Gelatin Hybrid Hydrogels Containing Doxorubicin Loaded Chitosan/AuNPs Nanogels for the Local Therapy of Breast Cancer. *Int. J. Biol. Macromol.* **2023**, *246*, 125640. [[CrossRef](#)]
90. Sabra, S.; Agwa, M.M. Lactoferrin, a Unique Molecule with Diverse Therapeutical and Nanotechnological Applications. *Int. J. Biol. Macromol.* **2020**, *164*, 1046–1060. [[CrossRef](#)] [[PubMed](#)]
91. Willis, M.S.; Parry, T.L.; Brown, D.I.; Mota, R.I.; Huang, W.; Beak, J.Y.; Sola, M.; Zhou, C.; Hicks, S.T.; Caughey, M.C.; et al. Doxorubicin Exposure Causes Subacute Cardiac Atrophy Dependent on the Striated Muscle-Specific Ubiquitin Ligase MuRF1. *Circ. Heart Fail.* **2019**, *12*, e005234. [[CrossRef](#)]
92. Dash, S.; Murthy, P.N.; Nath, L.; Chowdhury, P. Kinetic Modeling on Drug Release from Controlled Drug Delivery Systems. *Acta Pol. Pharm.-Drug Res.* **2010**, *67*, 217–223.
93. Ritger, P.L.; Peppas, N.A. A Simple Equation for Description of Solute Release II. Fickian and Anomalous Release from Swellable Devices. *J. Control. Release* **1987**, *5*, 37–42. [[CrossRef](#)]
94. Lakkakula, J.R.; Gujarathi, P.; Pansare, P.; Tripathi, S. A Comprehensive Review on Alginate-Based Delivery Systems for the Delivery of Chemotherapeutic Agent: Doxorubicin. *Carbohydr. Polym.* **2021**, *259*, 117696. [[CrossRef](#)]
95. Bergueiro, J.; Glitscher, E.A.; Calderón, M. A Hybrid Thermoresponsive Plasmonic Nanogel Designed for NIR-Mediated Chemotherapy. *Biomater. Adv.* **2022**, *137*, 212842. [[CrossRef](#)]
96. Huang, J.; Xue, Y.; Cai, N.; Zhang, H.; Wen, K.; Luo, X.; Long, S.; Yu, F. Efficient Reduction and PH Co-Triggered DOX-Loaded Magnetic Nanogel Carrier Using Disulfide Crosslinking. *Mater. Sci. Eng. C* **2015**, *46*, 41–51. [[CrossRef](#)] [[PubMed](#)]
97. Curcio, A.; Silva, A.K.A.; Cabana, S.; Espinosa, A.; Baptiste, B.; Menguy, N.; Wilhelm, C.; Abou-Hassan, A. Iron Oxide Nanoflowers@CuS Hybrids for Cancer Tri-Therapy: Interplay of Photothermal Therapy, Magnetic Hyperthermia and Photodynamic Therapy. *Theranostics* **2019**, *9*, 1288–1302. [[CrossRef](#)] [[PubMed](#)]
98. Espinosa, A.; Kolosnjaj-Tabi, J.; Abou-Hassan, A.; Plan Sangnier, A.; Curcio, A.; Silva, A.K.A.; Di Corato, R.; Neveu, S.; Pellegrino, T.; Liz-Marzán, L.M.; et al. Magnetic (Hyper)Thermia or Photothermia? Progressive Comparison of Iron Oxide and Gold Nanoparticles Heating in Water, in Cells, and In Vivo. *Adv. Funct. Mater.* **2018**, *28*, 1803660. [[CrossRef](#)]

Disclaimer/Publisher's Note: The statements, opinions and data contained in all publications are solely those of the individual author(s) and contributor(s) and not of MDPI and/or the editor(s). MDPI and/or the editor(s) disclaim responsibility for any injury to people or property resulting from any ideas, methods, instructions or products referred to in the content.